ACS APPLIED ENERGY MATERIALS

www.acsaem.org Article

Carbon Additive-Free Crumpled $Ti_3C_2T_X$ MXene-Encapsulated Silicon Nanoparticle Anodes for Lithium-Ion Batteries

Kasturi Sarang, Xiaofei Zhao, Dustin Holta, Huaixuan Cao, Kailash Arole, Paraskevi Flouda, Eun-Suok Oh, Miladin Radovic,* Micah J. Green,* and Jodie L. Lutkenhaus*

Cite This: *ACS Appl. Energy Mater.* 2021, 4, 10762–10773 Read Online

ACCESS | Metrics & More | Article Recommendations | Supporting Information

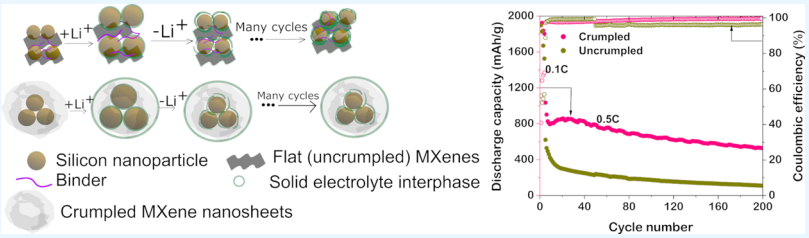

ABSTRACT: Silicon anodes are promising for future lithium-ion battery applications, but the large volume expansion of silicon particles causes electrode disintegration and excessive solid electrolyte interphase buildup during charge−discharge. This results in diminished cycling capacities and Coulombic efficiencies. "Yolk-shell" structures, wherein silicon particles are encapsulated within a conductive coating, have been explored in the recent past to address this issue, but most use amorphous carbon shells that have poor interactions with silicon. Here, conductive $Ti_3C_2T_X$ MXene nanosheets are crumpled around silicon particles via a one-step spray-drying process to create carbon-free anodes. The hydroxyl (−OH) terminal groups on the MXene surface contribute to the formation of a robust electrode via hydrogen bonding interactions with neighboring MXenes and encapsulated silicon particles. The relative silicon and MXene contents are varied to obtain crumpled MX/Si capsules of varying compositions, leading to different particle morphologies and energy storage performance metrics. The best-performing anode contains crumpled MX/Si = 32/68 wt % without any carbon additives required, demonstrating the cycling capacities of ∼550 mAh/g_{total} at a current density of ∼1.7 A/g_{total} (0.5 C-rate). Compared to equivalent electrodes containing uncrumpled MX/Si or crumpled reduced graphene oxide/Si, the crumpled MX/Si was far superior.

KEYWORDS: *silicon anodes, MXenes, spray dryer, crumpled, yolk-shell, carbon free, solid-electrolyte interface*

INTRODUCTION

The development of high energy density lithium-ion batteries (LiBs) is required to address the critical needs of applications including electronics, such as laptops, mobile phones, power tools, *etc.*, and electric vehicles.[1] Over time, the energy density of LiBs has gradually increased, but the current lithium-graphite (LiC_6) intercalation chemistries are approaching their limits.[2] To further increase the energy density, other high-capacity anode materials with alloying chemistries are being investigated.[3] Among those, silicon is regarded as an ideal anode because of its superior theoretical specific capacity of 3579 mAh/g ($Li_{15}Si_4$), low working potential (∼0.5 V *vs* Li/Li^+), and abundance in nature.[4]

Despite these advantages, silicon anodes have faced two major issues. First, silicon particles undergo >300% volumetric expansion upon full lithium insertion (lithiation).[5] This causes pulverization of silicon particles and subsequent loss of contact with active materials and the electrode framework. Second, due to the low electrochemical potential, a solid electrolyte interphase (SEI) layer deposits on the anode due to the reductive decomposition of the electrolyte.[6] Usually, a thin SEI layer formed during the first cycle prevents further electrolyte decomposition by passivating the anode surface. However, in the case of silicon anodes, the SEI layer repeatedly breaks due to silicon's expansion and contraction, which exposes new silicon surfaces to the electrolyte and causes continuous SEI buildup.[7] The excessive growth of the SEI increases cell resistance, lowers Coulombic efficiency, and consumes the electrolyte, all of which cause a rapid drop in the battery's capacity.[7]

Pioneering studies have shown that pulverization can be minimized by utilizing silicon particles of sizes less than 150 nm.[8] Based on these findings, numerous reports have utilized silicon nanoparticles,[1,9] nanowires,[10] and nanotubes.[11] Even

Received: June 16, 2021
Accepted: September 15, 2021
Published: October 8, 2021

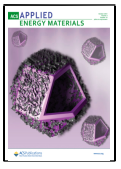

https://doi.org/10.1021/acsaem.1c01736
ACS Appl. Energy Mater. 2021, 4, 10762−10773

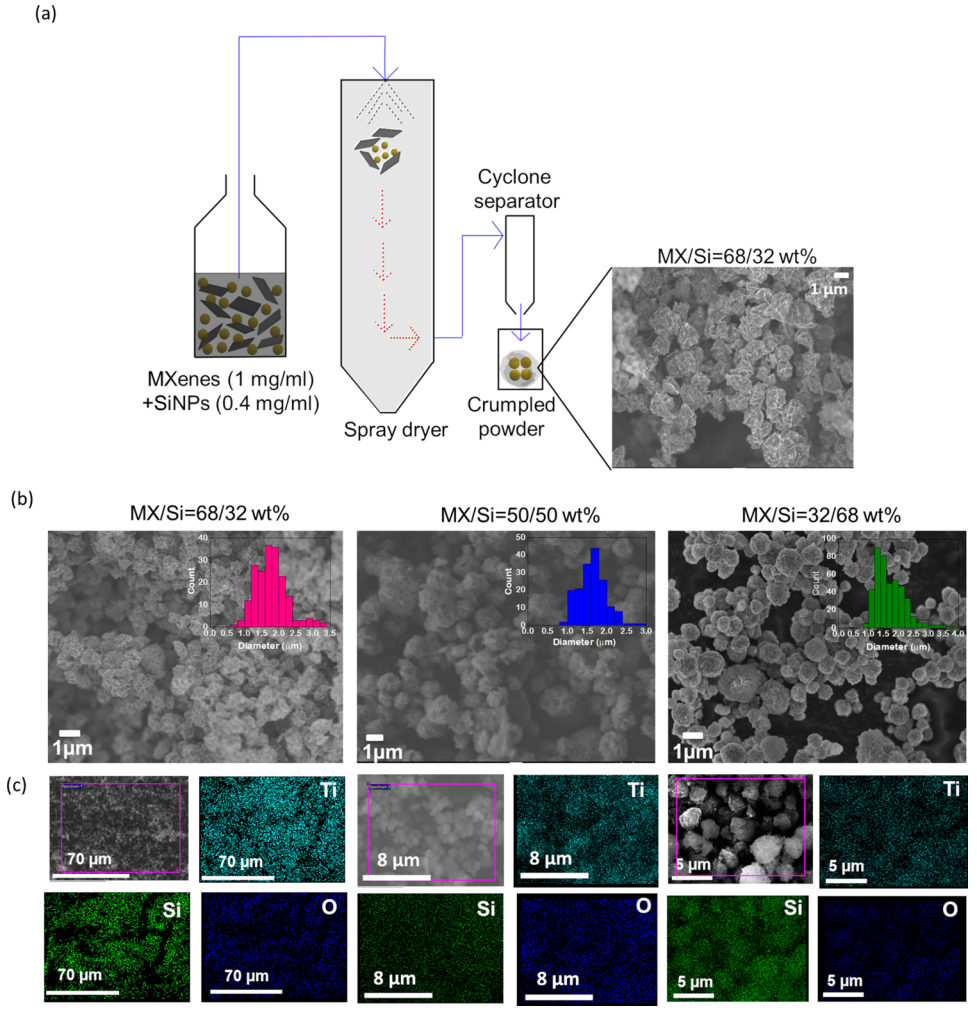

Figure 1. (a) Schematic of spray dryer assembly used to crumple MXene nanosheets around SiNPs and an SEM image of the crumpled product. A mixture of MXene nanosheets and SiNPs is spray-dried to obtain a crumpled product at the end of the cyclone separator. (b) SEM images of three different sets of spray-dried mixtures: MX/Si = 68/32, MX/Si = 50/50, and MX/Si = 32/68, in which the values represent the wt % of that component in the dispersion before spray drying. The inset shows histograms of crumpled particle sizes. (c) EDS of crumpled particles.

though the pulverization issue is minimized, the issues of delamination due to volume changes and continuous SEI buildup still persists. Thus, several other approaches have focused on core−shell (or yolk-shell)[12] and porous structures[13] that have both shown improved anode cycling stability due to the presence of interior void spaces or preformed porosity that buffer the changes in volume and stabilize SEI formation.[12,14]

Specifically, in the core−shell structure, the silicon active material is encapsulated within a conducting carbon layer, with void space provided between the carbon layer and the active material. Several methods have been used to make such core−shell structures, and the resulting anodes have shown improved capacities (400−1200 mAh/g at C-rates of 0.3−0.5 C, based on a mass of a yolk-shell capsule).[15−23] However, most of the previous studies utilized amorphous carbon or graphene shells that had poor interactions with silicon and with each other, owing to the lack of hydrogen bonding groups. This can lead to the disintegration of the capsule or of the electrode structure during long-term cycling.[24] Additionally, these studies have utilized multistep, lengthy procedures and/or high temperatures (500−800 °C). Thus, a simple one-step method to create such a yolk-shell structure is desired. Also, it is desirable to use conductive shells that have abundant hydrogen bonding groups, so as to form capsules that can preserve their structure during silicon's volume changes with cycling. For this, 2D transition metal carbides, specifically MXenes, show promise.

Two-dimensional (2D) MXene nanosheets have attracted recent attention in the field of energy storage because of their favorable combination of properties such as electronic conductivity, compositional adaptability, and pseudocapacitive charge storage.[25,26] $Ti_3C_2T_X$ (here, T_X represents MXene surface functional groups) is one such MXene material, which has a 2D structure similar to that of graphene but provides faster Li^+ transport ($\approx 10^{-10}-10^{-9}$ cm^2/s) due to the lower lithium diffusion barrier in MXenes (0.07 eV) versus that of graphene (0.3 eV).[27,28] Additionally, the MXene nanosheet surface has abundant hydrogen bonding groups (−OH, −O), which are favorable for interacting with silicon-active material.[29]

Several MXene-Si composites have been reported wherein silicon particles are sandwiched between MXene nanosheets via physical blending,[29−32] vacuum filtration,[33] electrostatic interactions,[34] and in situ magnesiothermic/aluminothermic reductions from MXene nanosheets−SiO_2 composites.[35,36] Recently, core−shell structures using MXene nanosheets and

https://doi.org/10.1021/acsaem.1c01736
ACS Appl. Energy Mater. 2021, 4, 10762−10773

silicon particles were also reported, but these prior reports used carbon additives (15−20 wt %) to maintain conductivity, thus increasing the dead weight in the anode.[24,37] Xia et al. prepared core−shell structures using a sacrificial method in which MXene nanosheets were wrapped around porous silicon nanospheres coated with a removable poly(methyl methacrylate) layer.[24] The electrodes demonstrated a long-term cycling capacity of ∼500 mAh/g (350 mAh/g_{total}) at the 2000th cycle at 0.2 C. These core−shell structures were synthesized using a complex, multistep process involving harsh chemicals and high temperatures. On the other hand, Yan et al. prepared core−shell MXene/Si (core−shell or yolk-shell-type MXene/Si structure is denoted as MX/Si here) structures using a spray dryer.[37] The electrodes showed capacities of 400 mAh/g_{total} at the 500th cycle at ∼0.5 C. Both of these studies utilized 30 wt % in total of binders and carbon additives, thus reducing the total electrode capacity and diluting the active silicon material. Reducing the quantity of "dead-weight" additives could, in principle, improve the total capacity of the anode.

Here, we designed a carbon additive-free anode containing MXenes crumpled around silicon particles using a simple one-step spray-drying process. These crumpled particles were blended with a poly(vinylidene fluoride) (PVdF) binder to fabricate electrodes with an aim to minimize the dead weight in the electrode. We determined the optimum content of MXenes and silicon particles to maximize the cycling capacity, which was 68 wt % silicon and 32 wt % MXenes. This optimum composition did not contain carbon additives, but PVdF was still needed as a binder to connect MX/Si capsules. To evaluate the battery performance, we performed galvanostatic cycling to determine the electrode's capacity and stability at higher C-rates, along with extended cycling. We performed electrochemical impedance spectroscopy to determine the electrode's impedance and cyclic voltammetry at different scan rates to deconvolute the charge-storage mechanism. We utilized scanning electron microscopy (SEM), along with energy-dispersive X-ray spectroscopy (EDS), to observe morphologies and elemental distribution, respectively. We also utilized X-ray photoelectron spectroscopy (XPS) to evaluate the SEI formed on the electrode after cycling. Additionally, we directly compared the crumpled electrode's performance with the uncrumpled electrode to correlate the observed performance with an electrode architecture.

EXPERIMENTAL SECTION

Materials. Silicon nanoparticles (>98% purity, 50−70 nm size, 80−120 m^2/g surface area) (SiNPs) were purchased from US-research nanomaterials. Poly(vinylidene fluoride) powder (Solef 5130) was purchased from Solvay. One mole lithium hexafluorophosphate ($LiPF_6$) in ethylene carbonate (EC):diethyl carbonate (DEC) (1:1 v/v), hydrochloric acid (HCl, ACS reagent 37% w/w), dimethyl sulfoxide (DMSO, ReagentPlus, >99.5%), sodium ascorbate (>99% assay), and 1-methyl-2-pyrrolidinone (ACS reagent, >99% purity) were purchased from Sigma-Aldrich. Lithium foil (0.75 mm thick × 19 mm wide), lithium fluoride (LiF, >98% purity), fluoroethylene carbonate (FEC), titanium (Ti, 44 μm average particle size, 99.5% purity), aluminum (Al, 44 μm average particle size, 99.5% purity), and titanium carbide (TiC) (2−3 μm average particle size, 99.5% purity) were purchased from Alfa Aesar. Super P carbon black (CB) (0.04 μm particle size, 62 m^2/g surface area) and copper foil (length × width × thickness = 170 m × 280 mm × 9 μm) were purchased from MTI corporation. A polypropylene separator (19 mm diameter × 0.025 mm thick) was purchased from Celgard.

Methods. *Preparation of MXenes Crumpled Around SiNPs.* $Ti_3C_2T_X$ MXene nanosheets were synthesized following a procedure available in the literature[38] and also detailed in the Supporting Information. The as-synthesized MXene nanosheet colloidal solution was treated with an equal molar amount of sodium ascorbate (NaASc) (*e.g.*, to 1 M colloidal solution of MXene nanosheets, 1 M NaASc was added) to minimize their oxidation and improve their stability in water.[39] Three different dispersions were prepared: MX = 1 mg/mL + Si = 0.6 mg/mL, MX = 1 mg/mL + Si = 0.4 mg/mL, and MX = 0.4 mg/mL + Si = 1 mg/mL. These dispersions were bath sonicated for 10 min followed by vortex mixing for 2 min to ensure the formation of a uniform and stable dispersion. These dispersions were passed through a spray dryer (Buchi B-290 mini spray dryer) to generate the crumpled product (Figure 1). For the spray-drying process, a pump flow rate of 10% (of maximum possible flow rate), atomizer air pressure of 60 psi, and an inlet temperature of 200 °C were used. The dispersion was atomized to form micrometer-sized droplets that were then mixed with in-house air that flowed through a vertical path, and the product was collected in a vessel after the cyclone separator (Figure 1a).

During spray drying, dispersions were stirred at 50 rpm to minimize the settling of SiNPs. The as-synthesized crumpled product was stored under vacuum at room temperature until further use.

Material Characterization. *Scanning Electron Microscopy (SEM) and Energy-Dispersive X-ray Spectroscopy (EDS).* The morphologies of the crumpled product and fabricated electrodes were characterized using SEM (JEOL JSM SEM) together with EDS. For SEM, an accelerating voltage of 5 kV and a working distance of 15 mm were applied. For EDS, an accelerating voltage of 20 kV and a working distance of 8 mm were applied. The EDS data were analyzed using INCA software. Prior to characterization, the samples were coated with platinum (3 nm) using a sputter coater (208 HR by Cressington). The size of the crumpled particles was determined by analyzing images using Image J software. To perform SEM analysis on electrodes after cycling, the electrodes were washed with dimethyl carbonate and dried at room temperature for 3−4 days.

X-ray Photoelectron Spectroscopy (XPS). XPS was performed (Omnicron XPS equipment) using a Mg source X-ray beam. XPS survey scans were performed with an analyzer pass energy of 100−1100 eV (1.0 eV steps, 50 ms dwell time). All spectra were calibrated with the C 1s photoemission peak for sp^2-hybridized carbon at 284.5 eV and the full width half-maximum (FWHM) was constrained. Curve fitting (using CasaXPS software) was conducted using a Gaussian-Lorentzian peak shape after Shirley-type background correction. CasaXPS software was used for component peak fitting. Spectra for all components were calibrated based on the carbon peak (C−C, 284.5 eV). Three major constraints were applied for fitting. First, the components of Ti 2p ($2p_{3/2}$ and $2p_{1/2}$) were constrained to an area ratio of 2:1 $2p_{3/2}$:$2p_{1/2}$. Second, full width half-maximum (FWHM) values were constrained. Finally, all binding energies (eV) were verified with previous literature results.[39−41]

Electrochemical Measurements. The working electrode was prepared by casting slurries of crumpled product and PVdF as a binder in NMP. No additional carbon black was added. First, a dispersion of 9 wt % PVDF in NMP was made by stirring and heating at 90 °C overnight. The desired amount of PVDF solution was mixed with crumpled product using a mortar and pestle to form uniform slurries. Those slurries were then cast onto copper foil and dried at 50 °C overnight, followed by vacuum at room temperature for 3 days. The electrode fabrication process is described in Figure S1. Sixteen millimeter electrodes were punched using a precision disc cutter (MTI). The loading of composite material (*i.e.*, MX/Si capsule) ranged from 1 to 1.5 mg/cm^2. Higher loadings of 1.8, 2.2, and 2.8 mg/cm^2 were also made. These electrodes were then used to make half cells in an argon-filled glovebox (MBRaun, Labstar). Lithium metal was used as the counter/reference electrode, 1 M $LiPF_6$ in EC:DEC (1:1 v/v) with 10 wt % FEC was used as the electrolyte (∼400 μL), and two 3501 Celgard separators were used.

All electrochemical testing was performed at room temperature (22−30 °C). Galvanostatic charge−discharge (GCD) tests and rate performance tests were performed using battery testing equipment (Arbin Instrument, HPT-100 mA) in a voltage window of 0.01−1 V

https://doi.org/10.1021/acsaem.1c01736
ACS Appl. Energy Mater. 2021, 4, 10762−10773

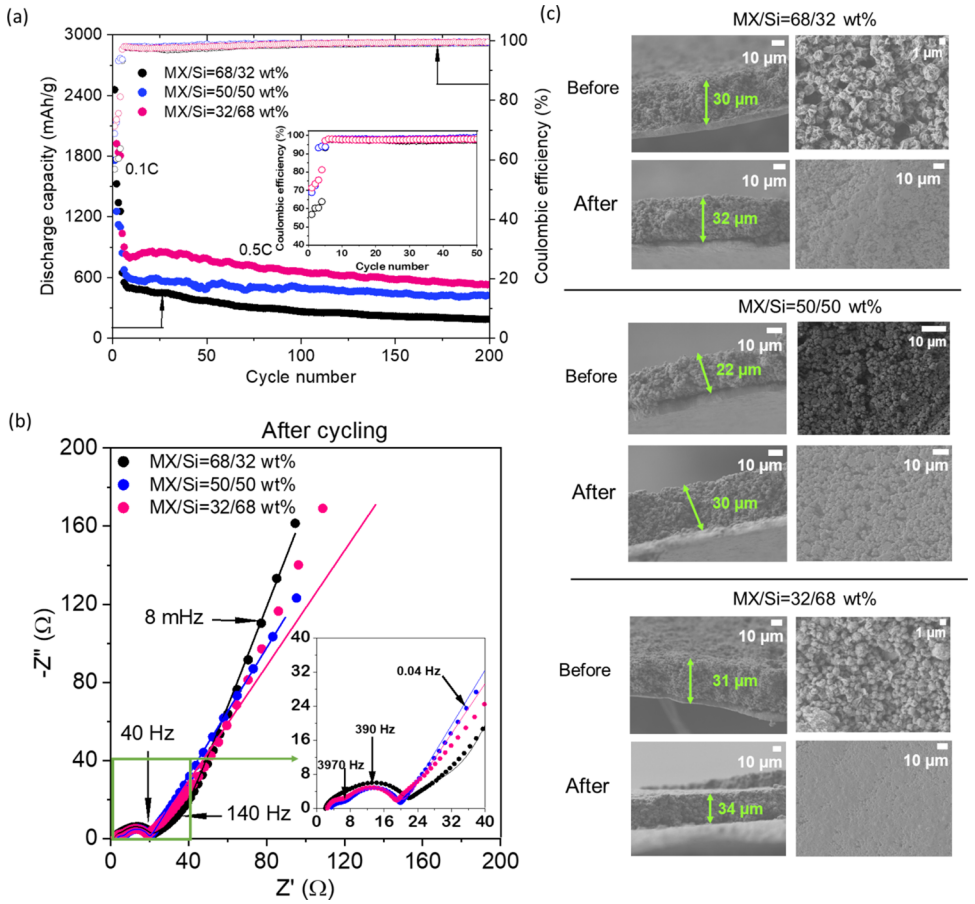

Figure 2. (a) Galvanostatic charge−discharge capacity for 200 cycles of MX/Si = 68/32, MX/Si = 50/50, and MX/Si = 32/68 electrodes with 5 wt % PVDF. The inset shows a zoomed-in plot of Coulombic efficiency *vs* cycle number for the first 50 cycles. (b) Nyquist plots (after 100 cycles of charge−discharge) of all three electrodes. The solid lines represent the equivalent circuit fit to the data. The inset shows a zoomed-in image of the green box. (c) SEM images of electrodes (surface and cross section) before and after 100 cycles. The cross-sectional SEM images also show the electrode thickness.

vs Li/Li^+. For GCD tests, cells were cycled at 0.1 C in constant current−constant voltage (CC−CV) mode for the first five cycles, followed by cycling at 0.5 C in CC mode for the remaining 195 cycles. In CV mode, the voltage was held constant at 0.01 V until the current decayed to 0.01 C. For rate performance tests, cells were cycled at different C-rates of 0.05, 0.1, 0.2, 0.5, 1, 2, and 3 C (at 0.05 C—three cycles, remaining C-rates—five cycles each), all in CC mode. The charge−discharge rates were calculated based on the theoretical capacity of silicon (3579 mAh/g). All capacities, unless specified, are reported based on the combined mass of the Si/MXene capsule. We also carried long-term cycling tests (500 cycles) at a constant C-rate of 0.1 C for selected electrodes. Cyclic voltammetry was performed (Solartron, Electrochemical Interface 1287) at different scan rates of 0.1, 0.2, 0.3, 0.4, 0.5, 0.7, and 0.9 mV/s (each for three cycles). Electrochemical impedance spectroscopy (EIS) was performed (Gamry Instruments, Electrochemical Interface 1000) with a 50 mV amplitude and 100 kHz to 5 mHz frequency range at a DC potential of 0.2 V *vs* Li/Li^+. Prior to EIS testing, the cell was conditioned at 0.2 V for 2 h.

RESULTS AND DISCUSSION

Spray drying was used to create MXene nanosheets crumpled around SiNPs, as shown in Figure 1, from a colloidal dispersion of $Ti_3C_2T_X$ MXene with the desired amount of SiNPs (sodium ascorbate was added to the colloidal dispersion to minimize oxidation of MXene nanosheets[39]). The crumpling of MXene nanosheets occurs because of capillary force action caused by the rapid evaporation of water from the mixture.[40] This structure is called "crumpled MXenes" because of its resemblance to a crumpled paper. Three sets of crumpled products were produced and were labeled according to the relative weight percentages of MXene and SiNP particles in the original dispersions: MX/Si = 68/32, MX/Si = 50/50, and MX/Si = 32/68. SEM and EDS were performed on the crumpled products to observe the morphology and distribution of MXenes and SiNPs. SEM images confirm the successful crumpling of MXene nanosheets around SiNPs. The particle sizes were 1−2.5 μm for all three compositions, Figure 1b. Figure S2 shows a high-magnification SEM image of crumpled MX/Si = 32/68 powder. We attribute the tight distribution to our past studies on optimizing spray-drying conditions to achieve relatively more uniform size distributions for graphene oxide.[42] EDS confirmed the presence of titanium (from MXenes) and silicon, as expected (Figure 1c, Figure S3, and Table S1). To verify the yolk-shell structure, we broke MX/Si capsules by sonication of an aqueous dispersion; Figure S4 shows individual Si particles and flat MXene nanosheets as products of opened capsules.

XRD analysis on crumpled MX/Si = 32/68 powder was used to verify the presence of MXenes and silicon nanoparticles (Figure S5). Strong diffraction peaks at 28.6, 47.5, 56.3, and 61.1° are assigned to the (111), (220), (311), and (400) planes of cubic Si crystal, respectively. The peak at 6.3° is

https://doi.org/10.1021/acsaem.1c01736
ACS Appl. Energy Mater. 2021, 4, 10762−10773

assigned to Ti_3C_2 MXenes. This shows that crumpling MXene nanosheets do not affect the crystal structure of nanosheets.[40]

From the preceding data, we estimated the number of SiNPs per capsule. We assumed that 7−8 MXene sheets (each ∼1 nm[29]) wrap around a cluster of SiNPs to form a capsule.[37] If the thickness of the capsule wall is ∼9−10 nm (∼1 nm × 8 layers of MXene sheets),[37] then the capsule wall's thickness may be considered negligible relative to the 1.5 μm capsule diameter. Assuming perfect spheres of diameters 1.5 μm and 60 nm for the capsule and the SiNP, respectively, as well as a 63% packing fraction, we estimate an upper bound of ∼9800 SiNPs per capsule. We expect the actual SiNP loading to decrease as the MXene weight fraction increases (and the particle size remains about the same).

XPS was also performed on crumpled products (Figure S6). The survey scans for all three crumpled products each show the presence of both titanium and silicon. The elemental composition and deconvoluted C 1s, O 1s, F 1s, Ti 2p, and Si 2p peaks were examined to show several features attributed to MXene nanosheets.[39,40] Figures S7−S9 show the presence of TiO_2 (∼460 eV) in the deconvoluted Ti spectra, which implies that some MXene nanosheets had oxidized.[40] The deconvoluted O spectra show the presence of a Si−O−Ti peak (∼531 eV).[24] Also, Si−O and Si−Si peaks at 102.3 and 99.8 eV, respectively, were observed in the deconvoluted Si spectra.

Having obtained three different compositions of MX/Si capsules, we next performed an initial screening to determine the minimal amount of PVdF binder required to form a carbon additive-free, crumpled MX/Si anode. The three sets of crumpled products were mixed with varying amounts of PVDF and slurry cast from NMP (organic solvent was used because MXenes uncrumple in the presence of water[40]). In the absence of PVdF, electrodes crumbled and could not be cycled, so electrodes containing 5, 10, and 20 wt % PVdF were examined. The surface morphologies of MX/Si = 68/32, MX/Si = 50/50, and MX/Si = 32/68 electrodes with 5, 10, and 20 wt % PVDF are shown in Figure S10. The electrodes were assembled in two-electrode half cells with lithium metal as the counter/reference electrode and 1 M $LiPF_6$ in EC:DEC (1:1 v/v) with 10 wt % FEC as the electrolyte. Galvanostatic charge−discharge (GCD) was performed at 0.1 C in constant current−constant voltage (CC−CV) mode first for five cycles, followed by cycling at 0.5 C in CC mode for 195 cycles. All capacities, unless specified, are reported based on the mass of the MX/Si capsules. As the PVDF content in the electrode increased from 5 to 20 wt % (Figure S11), a drop in discharge capacity was observed due to PVdF's insulating nature. This observation was further confirmed using electrochemical impedance spectroscopy (EIS) on MX/Si = 68/32 electrodes containing 5, 10, or 20 wt % PVdF after 100 cycles. (Figures S12 and S13). The resistance was lowest for the electrode containing 5 wt % PVdF; thus, we concluded that 5 wt % PVDF was sufficient to maintain the electrode's integrity while minimizing the charge-transfer resistance, and all further studies used that PVdF composition.

Figure 2 presents GCD, EIS, and SEM analysis for MX/Si = 68/32, MX/Si = 50/50, and MX/Si = 32/68 anodes containing 5 wt % PVdF binder. The anodes were cycled as described before with the goal of determining the effect of varying the MXene/SiNP ratio. Figure 2a shows the galvanostatic cycling performance, and the corresponding voltage profiles are shown in Figure S14. For the first cycle (Figure S14a), a flat plateau at 0.1 V was present due to the conversion of crystalline silicon (c-Si) to lithiated amorphous a-Li_xSi. The initial discharge capacities for MX/Si = 68/32, MX/Si = 50/50, and MX/Si = 32/68 electrodes were 2710, 2628, and 2610 mAh/g, respectively; likewise, the initial Coulombic efficiencies (ICEs) were 56.8, 68.8, and 71.3%. It should be noted that the capacities reported here are based on the mass of the MX/Si capsule. The ICE increased as the MXene content decreased and as the silicon content increased. Reasons for reduced ICE may include the trapping of Li^+ ions by surface functional groups on MXene nanosheets.[43] The voltage profiles for selected remaining cycles at 0.5 C are shown in Figure S14b−d; two plateaus were observed, which is consistent with lithiation and delithiation of silicon.[5] Figure S15 shows a zoomed-in image of the CE *vs* cycle number plot, where we observed stable CE values.

The three electrodes were then cycled galvanostatically at 0.1 C for the first five cycles, and then at 0.5 C for 195 cycles. At the conclusion of cycling, the MX/Si = 32/68 electrode showed the highest discharge capacity at 0.5 C (550 mAh/g_{total}), followed by MX/Si = 50/50 and MX/Si = 68/32 electrode (400 and 190 mAh/g_{total}, respectively).

EIS was performed on these electrodes after 100 charge−discharge cycles. The Nyquist plots in Figure 2b show EIS responses for the three electrodes consisting of two semicircles in the high- and medium-frequency regions (attributed to the SEI resistance (R_{SEI}) and the charge-transfer resistance (R_{CT}), respectively) followed by a Warburg tail in the low-frequency region (attributed to Li^+ ion diffusion). The values of R_{SEI}, R_{CT}, and the Li^+ ion diffusion coefficient were obtained by fitting an equivalent circuit (Figure S13, Table S2) to the data. The combined R_{CT} + R_{SEI} values for MX/Si = 68/32, MX/Si = 50/50, and MX/Si = 32/68 electrodes were 17.3, 16.9, and 16.7 Ω, respectively. A very minor difference in total resistance was observed for three-electrode compositions tested, within which the MX/Si = 32/68 electrode showed the lowest resistance of 16.7 Ω. This could be a possible contributing factor for higher capacities demonstrated by that electrode composition (Figure 2a). The individual R_{CT} and R_{SEI} values for all three electrodes are shown in Table S2. R_{CT} was the lowest for the electrode with the highest MXene content (68 wt %), and R_{CT} increased with decreasing MXene content. R_{SEI}, on the other hand, was lowest for the electrode with the lowest MXene content (32 wt %). These results suggest that increasing the MXene loading improves charge transfer but probably traps more Li^+ ions during cycling.[43] We also calculated solid-state Li^+ ion diffusion coefficients (D_{Li^+}) for electrodes from the Warburg tail in the EIS data. We did not observe a distinct trend in the diffusion coefficients: D_{Li^+} for MX/Si = 68/32 was 1.92 × 10^{-11} cm^2/s, MX/Si = 50/50 was 9.03 × 10^{-11} cm^2/s, and MX/Si = 32/68 was 2.17 × 10^{-11} cm^2/s. Therefore, the amount of MXene additive should be balanced to provide sufficient binding and conductive pathways for SiNPs while minimizing the value of R_{SEI}. Within this study, the MX/Si = 32/68 anode appears to capture this balance most effectively.

To further understand the morphology and the SEI development for electrodes, we performed cross-sectional- and surface-SEM analysis (Figure 2c) on MX/Si = 68/32, MX/Si = 50/50, and MX/Si = 32/68 electrodes before and after 100 cycles. All electrodes showed similar surface morphologies before cycling, consisting of tightly packed MX/Si capsules. This result indicates that the crumpled structure remained intact even after the vigorous mixing required for slurry preparation and electrode processing.

https://doi.org/10.1021/acsaem.1c01736
ACS Appl. Energy Mater. 2021, 4, 10762−10773

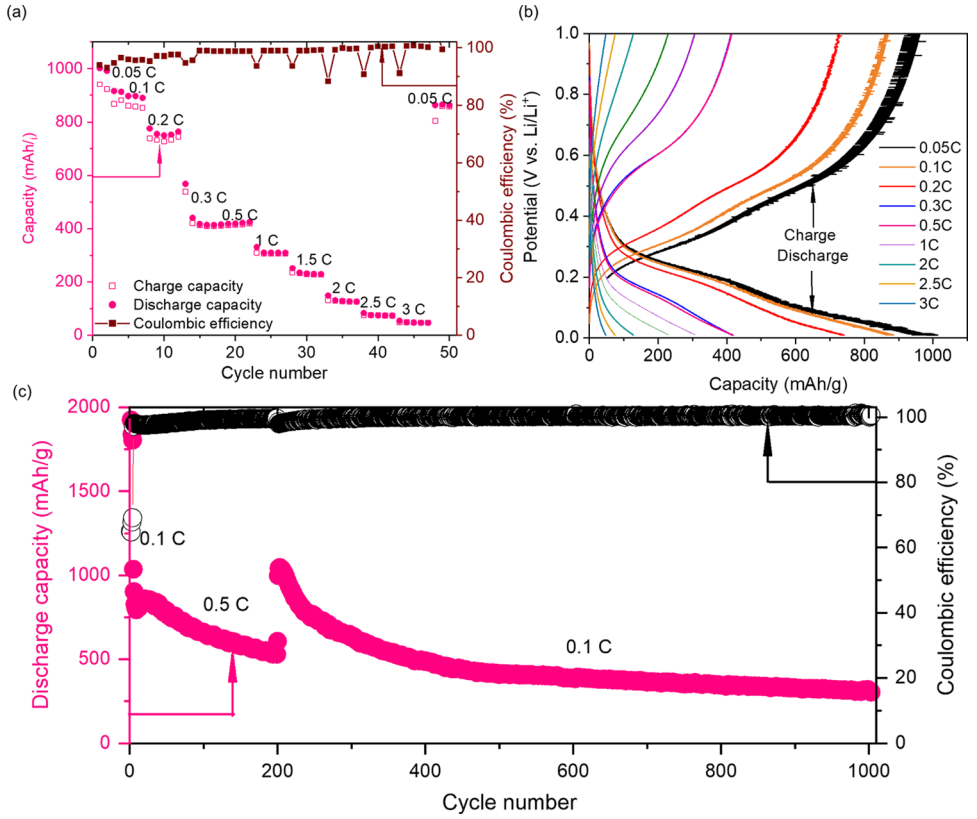

Figure 3. (a) Galvanostatic cycling and (b) voltage profiles at different C-rates ranging from 0.05 to 3 C for MX/Si = 32/68 electrode with 5 wt % PVdF (and no carbon additive). The voltage profile for the third cycle at each C-rate is shown. The electrode was cycled three times at 0.05 C-rate and five times each at the remaining C-rates. The C-rate was brought back to 0.05 C to determine capacity recovery. (c) Long-term galvanostatic cycling of a MX/Si = 32/68 electrode at C-rate of 0.1 C for the first five cycles in CC−CV mode, followed by cycling at 0.5 C in CC mode for 195 cycles, and then cycling at 0.1 C in CC mode for the remaining 800 cycles.

Cross-sectional SEM images allowed for the assessment of volume expansion, assuming expansion only through the thickness of electrode; specifically, MX/Si = 68/32, MX/Si = 50/50, and MX/Si = 32/68 electrodes expanded by 6.7, 36, and 9.6%, respectively, after 100 cycles. Since it is difficult to measure the electrode thickness of the entire electrode due to the limitations of SEM, we also measured thicknesses using a height gauge. The MX/Si = 68/32, MX/Si = 50/50, and MX/Si = 32/68 electrodes expanded by 22, 28, and 32%, respectively. Here, we observed a trend wherein the expansion increased as the MXene content increased. This trend can be explained as follows: for higher MXene weight fractions, the content of SiNPs in each capsule is lower and is more adaptable to changes in silicon's expansion within the capsule. The postcycling surface-SEM images for all three electrodes demonstrate the formation of an SEI layer that coats MX/Si capsules. Also, no noticeable cracks were observed in MX/Si electrodes (SEM images).

EDS was performed on MX/Si = 68/32, MX/Si = 50/50, and MX/Si = 32/68 electrodes before and after 100 cycles (Figure S16) to consider the SEI formation. Before cycling, the electrode surface shows a uniform distribution of Si, Ti, O, F, and Na elements. Trace amounts of Al were also observed. After cycling, all electrodes showed evidence of P (in addition to the elements observed on the surface before cycling) attributed to the SEI layer. Additionally, we observed that the wt % of Si and Ti on the electrode surface decreased after cycling, which further confirms the SEI formation.

Thus, our analysis shows that the MX/Si = 32/68 electrode has the highest discharge capacity, confirmed by the low charge-transfer resistance, improved the Coulombic efficiency, and low increase in electrode thickness after cycling. This can be attributed to the proper balance of MXene and SiNPs that allowed an expansion of SiNPs within the capsule without diluting the active Si material. Further, SEM analysis (Figure S17) confirmed the shelf-stability of the crumpled architecture, which stayed intact after 3 weeks of storage under vacuum and also after contacting with electrolyte. Therefore, all further electrochemical characterizations were performed on MX/Si = 32/68 anodes.

We next prepared electrodes with loadings of 1.8, 2.2, and 2.8 mg/cm^2, where the loading refers to the SiNP + MXene mass. We performed peel testing to determine the adhesion of these electrodes to the current collector (Figure S18). We observed that as the loading increased, the adhesion decreased. Further, the capacity decreased with increased loading, in which the electrodes with 1.8 and 2.8 mg/cm^2 demonstrated capacities of 400 and 280 mAh/g, respectively (Figure S19). Thus, we chose to make electrodes with an optimum mass loading of 1−1.5 mg/cm^2.

Also, we determined the tap density of crumpled Si/MX = 32/68 capsules (0.15 g/cm^3) and compared it to SiNPs (0.075 g/cm^3), Figure S20. A higher tap density of crumpled capsules implies that we can pack more material using the MX/Si capsule within the same electrode area, giving rise to much thinner electrodes.

https://doi.org/10.1021/acsaem.1c01736
ACS Appl. Energy Mater. 2021, 4, 10762−10773

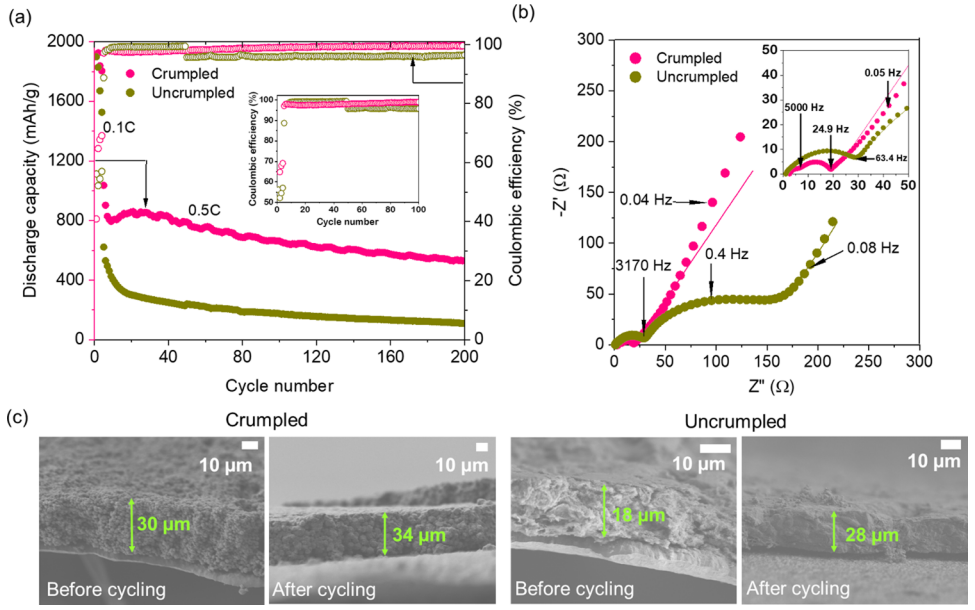

Figure 4. Comparison of (a) galvanostatic cycling MX/Si = 32/68 crumpled and noncrumpled electrodes. The inset shows a zoomed-in plot of Coulombic efficiency *vs* cycle number for the first 50 cycles. (b) Comparison of EIS (after 100 cycles of charge−discharge) of crumpled and noncrumpled electrodes. The inset shows a zoom-in of the Nyquist plot. (c) Cross-sectional scanning electron microscopy of MX/Si = 32/68 crumpled and noncrumpled electrodes before and after cycling.

Figure 3a,b shows the rate performance of MX/Si = 32/68 electrodes at different C-rates from 0.05 C to 3 C. The initial discharge capacity of the electrode at 0.05 C-rate was 1120 mAh/g, and it decreased to a capacity value of ∼780 mAh/g at the fifth cycle at 0.2 C. As the C-rate was further increased to 0.5 C, the capacity was reduced to a value of ∼420 mAh/g. The drop in capacity at high C-rates can be attributed to the diffusion barrier for Li^+ ions due to insufficient time for Li^+ ions to traverse the tortuous path presented by MXenes and/or due to diffusion limitation of Li^+ ions as typically observed for silicon anodes.[44] Almost 85% of the capacity was recovered when the C-rate was brought back to 0.5 C. This 15% loss in capacity can be attributed to electrical disconnection and/or due to SEI formation.[45,46]

To evaluate the MX/Si = 32/68 electrode stability over a large number of cycles, we performed GCD in CC−CV mode for the first five cycles, followed by cycling at 0.5 C in CC mode for 195 cycles, and then cycling at 0.1 C for the remaining 800 cycles. The C-rate was switched to 0.1 C after 200 cycles so as to minimize the degradation of lithium metal during long-term cycling, which occurs at high C-rates.[47] The electrode showed a discharge capacity value of ∼580 mAh/g at 200th cycle at 0.5 C. When the C-rate was lowered to 0.1 C, the capacity increased to 1015 mAh/g, which then stabilized to a value of ∼400 mAh/g. The initial Coulombic efficiency value was 65.5%, which increased to 97% within the first 10 cycles and then stabilized to a value of ∼99.8% at the final cycle. This long-term cycling stability and high CE values can be attributed to stable SEI formation and suppressed volumetric expansion due to effective wrapping of MXene nanosheets around SiNPs.

We next compared the galvanostatic cycling performance of our electrodes to other core−shell structured electrodes reported in the literature. We found that our electrodes demonstrated higher capacities than refs18, 19, 21, 24, 48−51 and lower capacities than refs15, 17, 22, 23, 37, 52−56 (based on the mass of a yolk-shell capsule, compared at similar C-rates). We specifically compared our electrode's performance to those reported by Yan et al. They fabricated electrodes using spray-dried Si/MXene capsules with 15 wt % NaCMC binder and 15 wt % Super P carbon black (CB) conductive additives and reported a capacity of ∼400 mAh/g_{total} at 500th cycle.[37] We made electrodes by adding just 5 wt % PVdF binder to our Si/MXene capsules (no carbon was added) and also observed a similar discharge capacity of ∼380 mAh/g_{total} at 1000th cycle at the same C-rate. We believe that using excessive binders and conductive additives can be avoided to further increase the total electrode capacity.

We also made an in-house comparison of MX/Si = 32/68 electrodes with and without Super P CB (Figure S21). We observed that the electrode with CB showed a lower discharge capacity (∼300 mAh/g) and ICE (54%) than the one without CB (discharge capacity ∼580 mAh/g, ICE = 71%). The postcycling surface-SEM images of the electrode with CB shows an uneven SEI layer, as opposed to a smooth SEI layer observed on the electrode without CB. The worse performance of the electrode with CB can be most likely attributed to inefficient packing of CB around MX/Si capsules, uneven distribution of CB, and excessive Li^+ ion trapping due to the presence of amorphous carbon, thus forming a thicker SEI layer.

Additionally, we compared the performance of spray-dried MX/Si capsules with rGO/Si capsules (Figure S22) to understand potential differences between rGO and MXene encapsulants. We fabricated crumpled rGO/Si = 32/68 electrodes following the same procedure as we used to make MX/Si = 32/68 electrodes (see the SI). The GCD data show that the rGO/Si = 32/68 electrode exhibited a capacity (350 mAh/g) lower than that of the MX/Si = 32/68 electrode (580 mAh/g). The EIS data further showed that rGO/Si = 32/68 electrodes bore a higher resistance as compared to the MX/Si = 32/68 electrode. This can be attributed to excessive SEI formation on exposed SiNPs in the rGO/Si = 32/68 electrode. rGO nanosheets have fewer surface hydroxyl groups, which are

https://doi.org/10.1021/acsaem.1c01736
ACS Appl. Energy Mater. 2021, 4, 10762−10773

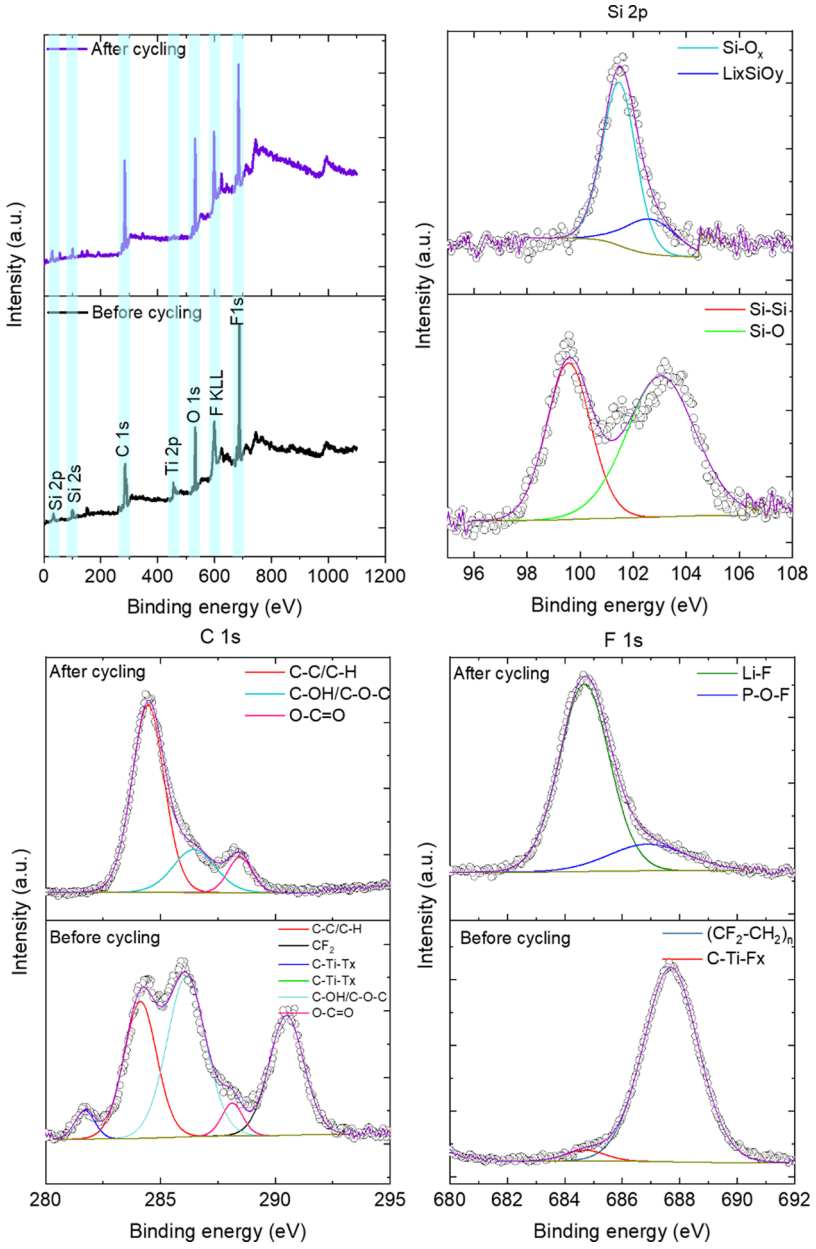

Figure 5. X-ray photoelectron spectroscopy of a crumpled MX/Si = 32/68 electrode before and after cycling.

needed for compatibilization with SiNPs. Finally, rGO has a higher Li^+ ion diffusion barrier than MXenes.[27,28] Taken together, these reasons may explain the superior performance of crumpled MX/Si electrodes vs analogous rGO ones.

We compared the performance of the crumpled MX/Si = 32/68 architecture to a noncrumpled one to understand the improvements brought about by crumpling. To make the noncrumpled electrode, 65 wt % SiNPs, 30 wt % MXene nanosheets, and 5 wt % PVDF were mixed to form a slurry which was cast on Cu foil. We observed that the crumpled electrode showed higher capacities (580 mAh/g) than the noncrumpled one (~200 mAh/g) (Figure 4a). This observation was further supported by EIS, where the $R_{CT} + R_{SEI}$ of the noncrumpled electrode (153 Ω) was higher than that of the crumpled electrode (16.7 Ω) (Table S2). Along with cycling performance, the rate performance of the uncrumpled electrode was worse when compared to the crumpled electrode (Figure S24). Surface-SEM images of the uncrumpled electrode revealed an undesirable patchy SEI layer (Figure S25). Cross-sectional SEM images after cycling show that the electrode thickness increased by ~55% for the noncrumpled electrode as opposed to 13% for the crumpled electrode. This shows that the crumpled electrode was able to alleviate volumetric expansion more effectively than the noncrumpled electrode. Taken together, this result shows the advantages of the crumpled architecture over the noncrumpled electrode.

To evaluate the SEI layer formed on the crumpled and uncrumpled MX/Si = 32/68 electrode's surface after cycling, we performed XPS analysis before and after 100 cycles (Figure 5, Figures S26–S28). The XPS survey scan of both the electrodes before cycling reveals the presence of C 1s, O 1s, F 1s, Si 2p, and Ti 2p, with the atomic% listed in Table S3. The deconvoluted C 1s spectra show the presence of the CF_2 (~292 eV) peak attributed to bonds present in PVdF binder along with C–C/C–H (284.5 eV), symmetric C–Ti–Tx (~281.7 and 280 eV), C–OH/C–O–C (~286.1), and O–

https://doi.org/10.1021/acsaem.1c01736
ACS Appl. Energy Mater. 2021, 4, 10762–10773

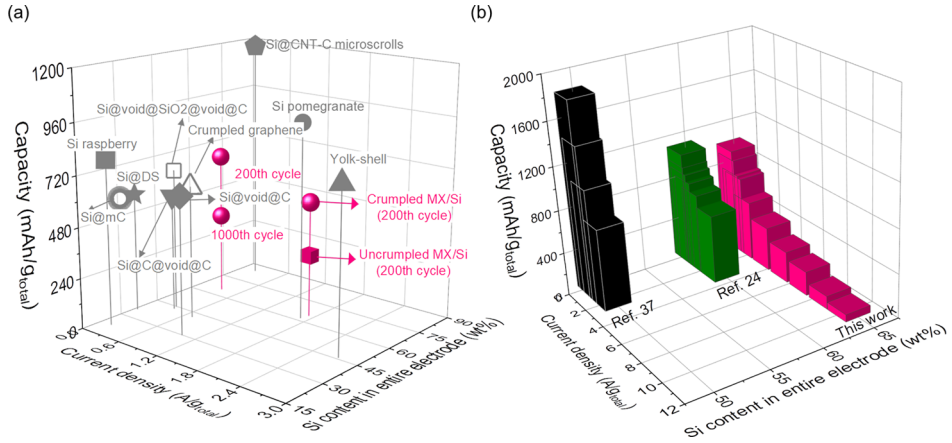

Figure 6. (a) Three-dimensional (3D) plot of electrode capacity (at *n*th cycle) (mAh/g_{total}), current (A/g_{total}), and Si content in the entire electrode comparing yolk-shell-type electrode architectures available in literature. (b) Three-dimensional (3D) plot of rate performance comparing yolk-shell-type Si/MXene architectures available in literature. Here, the mass of the total electrode is considered.

C═O (~288.1 eV) peaks from MXene nanosheets (Figure 5). The deconvoluted O 1s spectra for the crumpled MX/Si = 32/68 electrode shows peaks attributed to MXene nanosheets (C−Ti−OH_x ~531.2 eV, C−Ti−O_x ~530 eV, TiO_2 ~529.8 eV, Al_2O_3 ~532.7 eV, and H_2O ~533 eV) and a peak attributed to possible bond formation between SiNPs and MXene nanosheets (Si−O−Ti ~531.2 eV). We did not observe the Si−O−Ti peak for the case of the uncrumpled electrode. The deconvoluted F 1s peak shows the presence of C−F (~687.8 eV) and C−Ti−F_x (~684.7 eV), and deconvoluted Si 2p peak shows the presence of Si−Si (~99.8 eV) and Si−O (~103 eV) peaks. The deconvoluted Ti 2p peak shows several bonds that are typically present in MXene nanosheets.[40] The Ti peak was not distinctly observed for the case of an uncrumpled electrode and thus we did not deconvolute it further.

We then analyzed the peaks observed for both crumpled and uncrumpled electrodes after cycling. The XPS survey scans of both electrodes after cycling show the presence of Li 1s and P 2p, which is attributed to the SEI layer, in addition to the peaks observed before cycling. The deconvoluted peaks of Li, F, and P revealed the presence of LiF, Li_2CO_3, POF, Li_xSiO_y, $Li_xPO_yF_z$, Li_xPF_y, and SiO_x from the decomposition of EC, DEC, FEC, and $LiPF_6$ salt, which are typically observed in the silicon anode's SEI layer.[57−60] We observed a drop in the atomic% of Si, Ti, F, and C because of the SEI layer (Table S3).

Finally, we compared the long-term galvanostatic cycling performance (Figure 6a) and rate performance (Figure 6b) of our electrodes to those reported in literature. First, we compared the cycling performance of our electrodes to previous reports that used non-MXene core−shell geometries (Figure 6a). Generally, we observed that our crumpled MX/Si electrodes (data in pink) were able to achieve higher capacities at higher current densities (with a few exceptions[15,17]). Particularly, we noticed that we were able to obtain relatively high silicon content in our electrodes, with a few exemptions.[29,30,52] We also compared the cycling performance of our electrodes to previous reports that used flat (not core−shell) MXene-/Si constructs (Figure S29). The previously reported flat MXene/Si electrode showed higher capacities than ours, but their areal mass loading was lower (<1 mg_{total}/cm^2).

Second, we compared the rate performance with previously reported core−shell MX/Si electrodes (Figure 6b, electrode compositions are provided in Table S4). We chose a direct comparison of our data to two other reports because they, too, studied electrodes made with MX/Si capsules (but with lower silicon loadings). Here, the electrode performance reported by Yan et al.[37] was better, but our electrodes showed comparable performance to those reported by Xia et al.[24] However, our electrodes could sustain higher current densities (up to ~1.7 A/g_{total} or 0.5 C-rate). The plots of specific energies and power are provided in the Supporting Information (Figure S30).

CONCLUSIONS

Here, we prepared MXene/Si core−shell, crumpled particles for anodes using a one-step spray-drying procedure, and we compared the resulting anodes with rGO-based crumpled particles and with MXene/Si flat (uncrumpled) electrodes. The spray-drying technique is scalable and can be easily applied to other anodes where volumetric expansion and excessive SEI formation is an issue. We varied the Si/MX content in the capsule as well the PVdF binder content in the electrode to increase the active material loading. The highest capacities observed were for Si/MX = 32/68 wt % electrode with 5 wt % PVdF binder, which we attributed to the balance of MXene and SiNPs in a capsule. This balance allowed for achieving high Si loading without diluting the active material to a large extent. We showed that our crumpled electrodes demonstrated a specific energy of 550 mAh/g_{total} at a current density of 1.7 A/g_{total} (or 0.5 C-rate) at the 200th cycle for electrode loading of 1.5 mg/cm^2. We further showed that our crumpled electrodes bore a decent cycling capacity of ~400 mAh/g_{total} at the 200th cycle at a current density of 0.3 A/g_{total} (or 0.1 C-rate). *b*-Value analysis revealed that electrodes exhibited a dual-energy storage mechanism, wherein Si and MXenes stored Faradaic and non-Faradaic energy, respectively. We showed that MXenes are better than rGO as encapsulants for SiNPs. An in-house comparison of the crumpled architecture to the flat (uncrumpled) architecture revealed the advantages of wrapping MXenes around SiNPs, which minimized SEI formation and improved cycle life. Compared to previous literature on yolk-shell and flat Si-MX electrodes, our electrodes showed comparable cycling performance, but without the need for any added carbon, which then allowed us

https://doi.org/10.1021/acsaem.1c01736
ACS Appl. Energy Mater. 2021, 4, 10762−10773

to access higher current densities (up 1.7 A/g_{total}). We believe that the spray-drying technique to make capsules can be extended to several other types of MXenes and anode materials, thus presenting a promising path to the scalable preparation of anode materials for lithium-ion batteries.

■ ASSOCIATED CONTENT

Supporting Information

The Supporting Information is available free of charge at https://pubs.acs.org/doi/10.1021/acsaem.1c01736.

MXene synthesis, *b*-value analysis, and additional figures as mentioned in the main text (PDF)

■ AUTHOR INFORMATION

Corresponding Authors

Miladin Radovic − *Department of Materials Science & Engineering, Texas A&M University, College Station, Texas 77843, United States*; Email: mradovic@tamu.edu

Micah J. Green − *Artie McFerrin Department of Chemical Engineering, Texas A&M University, College Station, Texas 77843, United States; Department of Materials Science & Engineering, Texas A&M University, College Station, Texas 77843, United States*; orcid.org/0000-0001-5691-0861; Email: micah.green@tamu.edu

Jodie L. Lutkenhaus − *Artie McFerrin Department of Chemical Engineering, Texas A&M University, College Station, Texas 77843, United States; Department of Materials Science & Engineering, Texas A&M University, College Station, Texas 77843, United States*; orcid.org/0000-0002-2613-6016; Email: jodie.lutkenhaus@tamu.edu

Authors

Kasturi Sarang − *Artie McFerrin Department of Chemical Engineering, Texas A&M University, College Station, Texas 77843, United States*

Xiaofei Zhao − *Artie McFerrin Department of Chemical Engineering, Texas A&M University, College Station, Texas 77843, United States*; orcid.org/0000-0002-0593-8490

Dustin Holta − *Department of Materials Science & Engineering, Texas A&M University, College Station, Texas 77843, United States*

Huaixuan Cao − *Artie McFerrin Department of Chemical Engineering, Texas A&M University, College Station, Texas 77843, United States*

Kailash Arole − *Artie McFerrin Department of Chemical Engineering, Texas A&M University, College Station, Texas 77843, United States*; orcid.org/0000-0002-4516-889X

Paraskevi Flouda − *Department of Materials Science & Engineering, Texas A&M University, College Station, Texas 77843, United States*

Eun-Suok Oh − *School of Chemical Engineering, University of Ulsan, Ulsan 44611, South Korea*

Complete contact information is available at: https://pubs.acs.org/10.1021/acsaem.1c01736

Author Contributions

The manuscript was written through the contributions of all authors. All authors have given approval to the final version of the manuscript.

Funding

National Science Foundation under grant no. 1760859.

Notes

The authors declare no competing financial interest.

■ ACKNOWLEDGMENTS

This material is based upon the work supported by National Science Foundation under the grants 1604682 and 1760859. The authors thank the Material Characterization Facility at Texas A&M University for SEM and XPS characterizations.

■ REFERENCES

(1) Li, J.-Y.; Xu, Q.; Li, G.; Yin, Y.-X.; Wan, L.-J.; Guo, Y.-G. Research progress regarding Si-based anode materials towards practical application in high energy density Li-ion batteries. *Mater. Chem. Front.* **2017**, *1*, 1691−1708.

(2) Choi, J. W.; Aurbach, D. Promise and reality of post-lithium-ion batteries with high energy densities. *Nat. Rev. Mater.* **2016**, *1*, No. 16013.

(3) Aricò, A.; Bruce, P.; Scrosati, B.; et al. Nanostructured materials for advanced energy conversion and storage devices. *Nat. Mater.* **2005**, *4*, 366−377.

(4) Choi, S.; Wang, G. Advanced Lithium-Ion Batteries for Practical Applications: Technology, Development, and Future Perspectives. *Adv. Mater. Technol.* **2018**, *3*, No. 1700376.

(5) McDowell, M. T.; Lee, S. W.; Nix, W. D.; Cui, Y. 25th anniversary article: Understanding the lithiation of silicon and other alloying anodes for lithium-ion batteries. *Adv. Mater.* **2013**, *25*, 4966−85.

(6) Franco Gonzalez, A.; Yang, N.-H.; Liu, R.-S. Silicon anode design for lithium-ion batteries: Progress and perspectives. *J. Phys. Chem. C* **2017**, *121*, 27775−27787.

(7) Casimir, A.; Zhang, H.; Ogoke, O.; Amine, J. C.; Lu, J.; Wu, G. Silicon-based anodes for lithium-ion batteries: Effectiveness of materials synthesis and electrode preparation. *Nano Energy* **2016**, *27*, 359−376.

(8) Liu, X. H.; Zhong, L.; Huang, S.; Mao, S. X.; Zhu, T.; Huang, J. Y. Size-dependent fracture of silicon nanoparticles during lithiation. *ACS Nano* **2012**, *6*, 1522−1531.

(9) Liu, L.; Lyu, J.; Li, T.; Zhao, T. Well-constructed silicon-based materials as high-performance lithium-ion battery anodes. *Nanoscale* **2016**, *8*, 701−22.

(10) Zamfir, M. R.; Nguyen, H. T.; Moyen, E.; Lee, Y. H.; Pribat, D. Silicon nanowires for Li-based battery anodes: a review. *J. Mater. Chem. A* **2013**, *1*, 9566.

(11) Wu, H.; Chan, G.; Choi, J. W.; Ryu, I.; Yao, Y.; McDowell, M. T.; Lee, S. W.; Jackson, A.; Yang, Y.; Hu, L.; Cui, Y. Stable cycling of double-walled silicon nanotube battery anodes through solid-electrolyte interphase control. *Nat. Nanotechnol.* **2012**, *7*, 310−5.

(12) Ashuri, M.; He, Q.; Shaw, L. L. Silicon as a potential anode material for Li-ion batteries: where size, geometry and structure matter. *Nanoscale* **2016**, *8*, 74−103.

(13) Ryu, J.; Hong, D.; Lee, H.-W.; Park, S. Practical considerations of Si-based anodes for lithium-ion battery applications. *Nano Res.* **2017**, *10*, 3970−4002.

(14) Dou, F.; Shi, L.; Chen, G.; Zhang, D. Silicon/Carbon composite anode materials for lithium-ion batteries. *Electrochem. Energy Rev.* **2019**, *2*, 149−198.

(15) Liu, N.; Wu, H.; McDowell, M. T.; Yao, Y.; Wang, C.; Cui, Y. A yolk-shell design for stabilized and scalable li-ion battery alloy anodes. *Nano Lett.* **2012**, *12*, 3315−21.

(16) Ma, C.; Wang, Z.; Zhao, Y.; Li, Y.; Shi, J. A. Novel Raspberry-like Yolk-Shell Structured Si/C Micro/Nano-Spheres as High-Performance Anode Materials for Lithium-Ion Batteries. *J. Alloys Compd.* **2020**, *844*, No. 156201.

(17) Liu, N.; Lu, Z.; Zhao, J.; McDowell, M. T.; Lee, H. W.; Zhao, W.; Cui, Y. A pomegranate-inspired nanoscale design for large-volume-change lithium battery anodes. *Nat. Nanotechnol.* **2014**, *9*, 187−92.

(18) Ma, Y.; Tang, H.; Zhang, Y.; Li, Z.; Zhang, X.; Tang, Z. Facile synthesis of Si-C nanocomposites with yolk-shell structure as an anode for lithium-ion batteries. *J. Alloys Compd.* **2017**, *704*, 599−606.
(19) Su, L.; Xie, J.; Xu, Y.; Wang, L.; Wang, Y.; Ren, M. Preparation and lithium storage performance of yolk-shell Si@void@C nanocomposites. *Phys. Chem. Chem. Phys.* **2015**, *17*, 17562−5.
(20) Sun, Z.; Song, X.; Zhang, P.; Gao, L. Controlled Synthesis of Yolk−Mesoporous Shell Si@SiO2 Nanohybrid Designed for High Performance Li Ion Battery. *RSC Adv.* **2014**, *4*, 20814−20820.
(21) Xie, J.; Tong, L.; Su, L.; Xu, Y.; Wang, L.; Wang, Y. Core-shell yolk-shell Si@C@Void@C nanohybrids as advanced lithium ion battery anodes with good electronic conductivity and corrosion resistance. *J. Power Sources* **2017**, *342*, 529−536.
(22) Yang, J.; Wang, Y.-X.; Chou, S.-L.; Zhang, R.; Xu, Y.; Fan, J.; Zhang, W.-x.; Kun Liu, H.; Zhao, D.; Xue Dou, S. Yolk-shell silicon-mesoporous carbon anode with compact solid electrolyte interphase film for superior lithium-ion batteries. *Nano Energy* **2015**, *18*, 133−142.
(23) Tao, H.; Fan, L. Z.; Song, W. L.; Wu, M.; He, X.; Qu, X. Hollow core-shell structured Si/C nanocomposites as high-performance anode materials for lithium-ion batteries. *Nanoscale* **2014**, *6*, 3138−42.
(24) Xia, M.; Chen, B.; Gu, F.; Zu, L.; Xu, M.; Feng, Y.; Wang, Z.; Zhang, H.; Zhang, C.; Yang, J. Ti3C2Tx MXene nanosheets as a robust and conductive tight on Si anodes significantly enhance electrochemical lithium storage performance. *ACS Nano* **2020**, *14*, 5111−5120.
(25) Naguib, M.; Mochalin, V. N.; Barsoum, M. W.; Gogotsi, Y. 25th Anniversary Article: MXenes: A New Family of Two-Dimensional Materials. *Adv. Mater.* **2014**, *26*, 992−1005.
(26) Naguib, M.; Kurtoglu, M.; Presser, V.; Lu, J.; Niu, J.; Heon, M.; Hultman, L.; Gogotsi, Y.; Barsoum, M. W. Two-dimensional nanocrystals produced by exfoliation of Ti3AlC2. *Adv. Mater.* **2011**, *23*, 4248−53.
(27) Tang, Q.; Zhou, Z.; Shen, P. Are MXenes promising anode materials for Li ion batteries? Computational studies on electronic properties and Li storage capability of Ti3C2 and Ti3C2X2 (X = F, OH) monolayer. *J. Am. Chem. Soc.* **2012**, *134*, 16909−16916.
(28) Kong, F.; He, X.; Liu, Q.; Qi, X.; Zheng, Y.; Wang, R.; Bai, Y. Effect of Ti3AlC2 precursor on the electrochemical properties of the resulting MXene Ti3C2 for Li-ion batteries. *Ceram. Int.* **2018**, *44*, 11591−11596.
(29) Sarang, K. T.; Zhao, X.; Holta, D.; Radovic, M.; Green, M. J.; Oh, E. S.; Lutkenhaus, J. L. Minimizing two-dimensional Ti3C2Tx MXene nanosheet loading in carbon-free silicon anodes. *Nanoscale* **2020**, *12*, 20699−20709.
(30) Zhang, C. J.; Park, S. H.; Seral-Ascaso, A.; Barwich, S.; McEvoy, N.; Boland, C. S.; Coleman, J. N.; Gogotsi, Y.; Nicolosi, V. High capacity silicon anodes enabled by MXene viscous aqueous ink. *Nat. Commun.* **2019**, *10*, No. 849.
(31) Kong, F.; He, X.; Liu, Q.; Qi, X.; Sun, D.; Zheng, Y.; Wang, R.; Bai, Y. Enhanced reversible Li-ion storage in Si@Ti3C2 MXene nanocomposite. *Electrochem. Commun.* **2018**, *97*, 16−21.
(32) Zhu, X.; Shen, J.; Chen, X.; Li, Y.; Peng, W.; Zhang, G.; Zhang, F.; Fan, X. Enhanced cycling performance of Si-MXene nanohybrids as anode for high performance lithium ion batteries. *Chem. Eng. J.* **2019**, No. 122212.
(33) Tian, Y.; An, Y.; Feng, J. Flexible and freestanding silicon/MXene composite papers for high-performance lithium-ion batteries. *ACS Appl. Mater. Interfaces* **2019**, *11*, 10004−10011.
(34) Zhang, F.; Jia, Z.; Wang, C.; Feng, A.; Wang, K.; Hou, T.; Liu, J.; Zhang, Y.; Wu, G. Sandwich-like silicon/Ti3C2Tx MXene composite by electrostatic self-assembly for high performance lithium ion battery. *Energy* **2020**, No. 117047.
(35) Hui, X.; Zhao, R.; Zhang, P.; Li, C.; Wang, C.; Yin, L. Low-temperature reduction strategy synthesized Si/Ti3C2 MXene composite anodes for high-performance Li-ion batteries. *Adv. Energy Mater.* **2019**, *9*, No. 1901065.
(36) Zhang, Y.; Mu, Z.; Lai, J.; Chao, Y.; Yang, Y.; Zhou, P.; Li, Y.; Yang, W.; Xia, Z.; Guo, S. MXene/Si@SiO x@C layer-by-layer superstructure with autoadjustable function for superior stable lithium storage. *ACS Nano* **2019**, *13*, 2167−2175.
(37) Yan, Y.; Zhao, X.; Dou, H.; Wei, J.; Sun, Z.; He, Y. S.; Dong, Q.; Xu, H.; Yang, X. MXene frameworks promote the growth and stability of LiF-rich solid-electrolyte interphases on silicon nanoparticle bundles. *ACS Appl. Mater. Interfaces* **2020**, *12*, 18541−18550.
(38) Alhabeb, M.; Maleski, K.; Anasori, B.; Lelyukh, P.; Clark, L.; Sin, S.; Gogotsi, Y. Guidelines for synthesis and processing of two-dimensional titanium carbide (Ti3C2Tx MXene). *Chem. Mater.* **2017**, *29*, 7633−7644.
(39) Zhao, X.; Vashisth, A.; Prehn, E.; Sun, W.; Shah, S. A.; Habib, T.; Chen, Y.; Tan, Z.; Lutkenhaus, J. L.; Radovic, M.; Green, M. J. Antioxidants nnlock shelf-stable Ti3C2TX (MXene) nanosheet dispersions. *Matter* **2019**, *1*, 513−526.
(40) Shah, S. A.; Habib, T.; Gao, H.; Gao, P.; Sun, W.; Green, M. J.; Radovic, M. Template-free 3D titanium carbide (Ti3C2Tx) MXene particles crumpled by capillary forces. *Chem. Commun.* **2017**, *53*, 400−403.
(41) Echols, I. J.; An, H.; Zhao, X.; Prehn, E. M.; Tan, Z.; Radovic, M.; Green, M. J.; Lutkenhaus, J. L. pH-Response of polycation/Ti3C2Tx MXene layer-by-layer assemblies for use as resistive sensors. *Mol. Syst. Des. Eng.* **2020**, *5*, 366−375.
(42) Parviz, D.; Metzler, S. D.; Das, S.; Irin, F.; Green, M. J. Tailored crumpling and unfolding of spray-dried pristine graphene and graphene oxide sheets. *Small* **2015**, *11*, 2661−8.
(43) Cheng, R.; Hu, T.; Zhang, H.; Wang, C.; Hu, M.; Yang, J.; Cui, C.; Guang, T.; Li, C.; Shi, C.; Hou, P.; Wang, X. Understanding the lithium storage mechanism of Ti3C2Tx MXene. *J. Phys. Chem. C* **2018**, *123*, 1099−1109.
(44) Tritsaris, G. A.; Zhao, K.; Okeke, O. U.; Kaxiras, E. Diffusion of Lithium in Bulk Amorphous Silicon: A Theoretical Study. *J. Phys. Chem. C* **2012**, *116*, 22212−22216.
(45) Radvanyi, E.; Porcher, W.; De Vito, E.; Montani, A.; Franger, S.; Jouanneau Si Larbi, S. Failure mechanisms of nano-silicon anodes upon cycling: an electrode porosity evolution model. *Phys. Chem. Chem. Phys.* **2014**, *16*, 17142−53.
(46) Yoon, T.; Nguyen, C. C.; Seo, D. M.; Lucht, B. L. Capacity fading mechanisms of silicon nanoparticle negative electrodes for lithium ion batteries. *J. Electrochem. Soc.* **2015**, *162*, A2325−A2330.
(47) Choi, S.; Kwon, T.-w.; Coskun, A.; Choi, J. W. Highly elastic binders integrating polyrotaxanes for silicon microparticles anode in Li ion batteries. *Science* **2017**, *357*, 279−283.
(48) Yang, L. Y.; Li, H. Z.; Liu, J.; Sun, Z. Q.; Tang, S. S.; Lei, M. Dual yolk-shell structure of carbon and silica-coated silicon for high-performance lithium-ion batteries. *Sci. Rep.* **2015**, *5*, No. 10908.
(49) Sun, Z.; Song, X.; Zhang, P.; Gao, L. Controlled synthesis of yolk−mesoporous shell Si@SiO2nanohybrid designed for high performance Li ion battery. *RSC Adv.* **2014**, *4*, 20814−20820.
(50) Sun, Z.; Tao, S.; Song, X.; Zhang, P.; Gao, L. A silicon/double-shelled carbon yolk-like nanostructure as high-performance anode materials for lithium-ion battery. *J. Electrochem. Soc.* **2015**, *162*, A1530−A1536.
(51) Zhou, X.-y.; Tang, J.-j.; Yang, J.; Xie, J.; Ma, L.-l. Silicon@carbon hollow core−shell heterostructures novel anode materials for lithium ion batteries. *Electrochim. Acta* **2013**, *87*, 663−668.
(52) Wang, H.; Fu, J.; Wang, C.; Wang, J.; Yang, A.; Li, C.; Sun, Q.; Cui, Y.; Li, H. A binder-free high silicon content flexible anode for Li-ion batteries. *Energy Environ. Sci.* **2020**, *13*, 848−858.
(53) Luo, J.; Zhao, X.; Wu, J.; Jang, H. D.; Kung, H. H.; Huang, J. Crumpled graphene-encapsulated Si nanoparticles for lithium ion battery anodes. *J. Phys. Chem. Lett.* **2012**, *3*, 1824−9.
(54) Lin, D.; Lu, Z.; Hsu, P.-C.; Lee, H. R.; Liu, N.; Zhao, J.; Wang, H.; Liu, C.; Cui, Y. A high tap density secondary silicon particle anode fabricated by scalable mechanical pressing for lithium-ion batteries. *Energy Environ. Sci.* **2015**, *8*, 2371−2376.

https://doi.org/10.1021/acsaem.1c01736
ACS Appl. Energy Mater. 2021, 4, 10762−10773

(55) Ma, C.; Wang, Z.; Zhao, Y.; Li, Y.; Shi, J. A novel raspberry-like yolk-shell structured Si/C micro/nano-spheres as high-performance anode materials for lithium-ion batteries. *J. Alloys Compd.* **2020**, 844.
(56) Chen, S.; Gordin, M. L.; Yi, R.; Howlett, G.; Sohn, H.; Wang, D. Silicon core-hollow carbon shell nanocomposites with tunable buffer voids for high capacity anodes of lithium-ion batteries. *Phys. Chem. Chem. Phys.* **2012**, *14*, 12741−5.
(57) Li, Q.; Liu, X.; Han, X.; Xiang, Y.; Zhong, G.; Wang, J.; Zheng, B.; Zhou, J.; Yang, Y. Identification of the solid electrolyte interface on the Si/C composite anode with FEC as the additive. *ACS Appl. Mater. Interfaces* **2019**, *11*, 14066−14075.
(58) Xu, Y.; Swaans, E.; Chen, S.; Basak, S.; R M L Harks, P. P.; Peng, B.; Zandbergen, H. W.; Borsa, D. M.; Mulder, F. M. A high-performance Li-ion anode from direct deposition of Si nanoparticles. *Nano Energy* **2017**, *38*, 477−485.
(59) Veith, G. M.; Doucet, M.; Sacci, R. L.; Vacaliuc, B.; Baldwin, J. K.; Browning, J. F. Determination of the Solid Electrolyte Interphase Structure Grown on a Silicon Electrode Using a Fluoroethylene Carbonate Additive. *Sci. Rep.* **2017**, *7*, No. 6326.
(60) Schroder, K. W.; Celio, H.; Webb, L. J.; Stevenson, K. J. Examining solid electrolyte interphase formation on crystalline silicon electrodes: influence of electrochemical preparation and ambient exposure conditions. *J. Phys. Chem. C* **2012**, *116*, 19737−19747.

https://doi.org/10.1021/acsaem.1c01736
ACS Appl. Energy Mater. 2021, 4, 10762−10773